Research Article

Numerical Simulation on the Influence of Injection Location, Injection Angle, and Divergence Half Angle on SITVC Nozzle Flow Field

H. R. Noaman [iD],[1] **Hai Bin Tang** [iD],[2] **and Elsayed Khalil** [iD][3]

[1]*School of Astronautics, Beihang University, Beijing, China*
[2]*School of Space and Environment, Beihang University, Beijing, China*
[3]*Aerospace Department, Military Technical College, Cairo, Egypt*

Correspondence should be addressed to H. R. Noaman; hossamnoaman84@outlook.com and Hai Bin Tang; thb@buaa.edu.cn

A numerical study has been performed to characterize the nozzle flow field of secondary injection thrust vector control (SITVC) and to estimate the performance parameters of SITVC. After validating the CFD turbulence models with an experimental data, a numerical simulation has been conducted in order to investigate the influence of changing the injection location, the injection angle, and the primary nozzle divergence half angle on the SITVC nozzle flow field structure and on the SITVC performance parameters. The secondary mass flow rate was kept constant for all cases during the simulation. The results showed that downstream injection near the nozzle exit $M_p = 2.75$ increases the high-pressure zone upstream the injection leading to an increase in the side force; also, the higher divergence half angle 15° slightly increases the side force and it provides a wide range of deflection without shock impingement on the opposite wall becoming more effective for SITVC. The injection angle in the upstream direction 135° increases the side force, and by decreasing the injection angle to downstream direction 45°, the side force decreases. However, the SITVC performance parameters and the flow field structure are more influenced by the injection location and the primary nozzle divergence half angle while being less influenced by the injection angle.

1. Introduction

Thrust vector control (TVC) is a way that controls the thrust by deflecting the main flow of a rocket motor or jet engine from the main axis to generate a specified force on the desired axis. As a result of this imbalance, a side force arises to be used in controlling the attitude of the aerial vehicle. Thrust vector control greatly enhances maneuverability, especially at low velocities or high angles of attack where conventional aerodynamic control surfaces are not effective. The thrust can be controlled mechanically by using flex joints, hinged nozzles, jetavators, and jet vanes/tabs or by fluidic thrust vector (FTV) control. In contrast to the mechanical systems that need actuators to move the mechanical parts leading to complex design and weight penalty, fluidic thrust vector control is a technology with less weight, faster dynamic response, and no mechanical movable parts and is

controlled by flow regulations, which decreases the axial thrust losses during a change in the direction of the thrust [1, 2]. There are different techniques of fluidic thrust vector control such as secondary injection thrust vector control (SITVC) or shock vector control (SVC), counter flow, Coanda effect, and throat skewing [3, 4].

From these techniques, SITVC is the most straightforward and effective technique of FTV [5, 6]. Since the 1960s, SITVC has been used successfully and is achieved by the injection of secondary fluid at the divergent part of the nozzle to the supersonic flow inside. The injection creates a complicated flow field in the divergent part of the nozzle upstream and downstream the injection where the upstream part contains a strong bow shock that creates asymmetry in the nozzle flow field, a weak separation shock, and two rotating vortices between the separation and the wall known as primary upstream vortex (PUV) and secondary upstream vortex
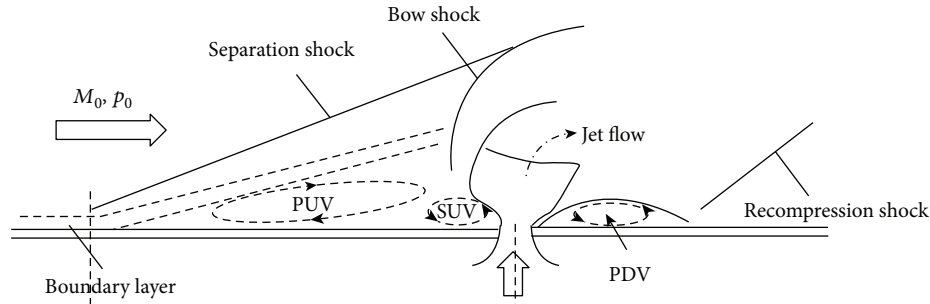
Figure 1: Structure of nozzle flow field with SITVC [12].

(SUV) as a result of the separation that occurs in the boundary layer; in the downstream part there are a Mach disk that recompress the under-expanded secondary fluid and a reattachment zone with recompression that contains primary downstream vortices (PDV) [7–11]. Figure 1 illustrates the SITVC nozzle flow field structure [12]. The main reason for the deflection is the side force which is generated by a combination of the interaction force (due to a rise in the pressure along the injector wall) and the jet reaction force (as a result of the momentum of the secondary injection) [13].

Many analytical models as Linearized model [14], blast-wave analogy [9], and boundary layer separation model [15], characterized the flow field that is induced due to a secondary fluid interaction with supersonic flow, but due to its complexity, these analytical models have lack in general and deal only with very low injection flow rates, so experimental tests with cold flow [16, 17] and real static firing [18, 19] were utilized to provide the SITVC main data. However, experimental tests only provide macroscopic SITVC performance predictions with high costs. On the other hand, development of numerical methods and computational power results in the development of computational fluid dynamics (CFD) to give a microscopic detailed description and analysis of the flow characteristics. Numerical simulation gives accurate results, which can be a strong complementary to experimental work [20, 21].

Balu et al. [7] solved the Euler equations for the estimation of the secondary injection performance parameters. Dhinagram and Bose [22] solved both Navier-Stokes and Euler equations in two-dimensional nozzles concluding that solving Navier-Stokes equations gives more accuracy to the results. Ko and Yoon [23] present a flow analysis of SITVC by solving three-dimensional Navier stokes equations with the Baldwin-Lomax turbulence model and $k - \varepsilon$ turbulence model. Sriram and Mathew [24] used the fluent code to simulate the flow field of the nozzle utilized by Masuya et al. [16] and Ko and Yoon [23] with different solution parameters. Vishnu et al. [25] used the realizable $k - \varepsilon$ turbulence model with enhanced wall treatment for the design optimization of SVC. Zmijanovic et al. [26] investigated experimentally and numerically the effects of FTV within the framework of a small satellite launcher. Prince Raj et al. [27] used a fluent code to solve the three-dimensional governing equations to analyze the flow field produced by secondary hot gas injection in a nozzle rocket motor. Rajendran et al. [28] carried out numerical studies using the two-dimensional RNG $k - \varepsilon$

turbulence model to compare between injecting sonic and supersonic jets for thrust vector control. Sellam et al. [5] analyzed the thermodynamic characteristics of the injected gas on FTV performance. Deng et al. [29] established an analytical model for transverse injection and performed a numerical model for secondary injection to study the thrust vectoring efficiency and system thrust ratio. Erdem and Kontis [30] carried out numerical simulations and experiments to analyze the transverse injection, then Erdem et al. [31] investigated experimentally the penetration characteristics of the transverse sonic jets in Mach 5 cross flows for air, carbon dioxide, and helium. Forghany et al. [32] studied numerically the effect of the fluidic injection angle on TVC system efficiency. Chandra Sekar et al. [33] carried out an experimental work to achieve FTV in the yaw direction by transverse injection in a converging nozzle with an elliptic exit and triangular after.

Although there are several researches on SITVC, there are rare investigations on the influence of the injection angle (downstream, perpendicular, and upstream inclination) and the primary nozzle divergence half angle on both the flow field structure and the performance parameters of SITVC. As a result, the current study is aimed at presenting a detailed qualitative analysis (without changing the secondary mass flow rate) on the influence of injection angle and primary nozzle divergence half angle on the SITVC flow field structure and performance parameters; also, the influence of injection location was investigated in order to investigate all the geometric parameters in the present study.

2. Numerical Methodology

Numerical simulation of the nozzle flow field in the presence of secondary injection has been performed. For this objective, Reynolds-averaged Navier–Stokes (RANS) equations, compressible, two-dimensional equations discretized in a finite volume form on each of the quadrilateral control volumes, were solved. An implicit density-based algorithm was utilized to solve the equations; for the flux type, Roe-averaged flux difference splitting (Roe FDS) was selected, and for the spatial discretization at the beginning, a first-order upwind scheme was chosen until a convergence behavior is shown, then a second-order upwind scheme was selected to increase the accuracy of the solution. The Courant-Friedrichs-Lewy (CFL) number starts with a small value of 0.5 to ensure the solution stability until a convergence behavior appears. Then,
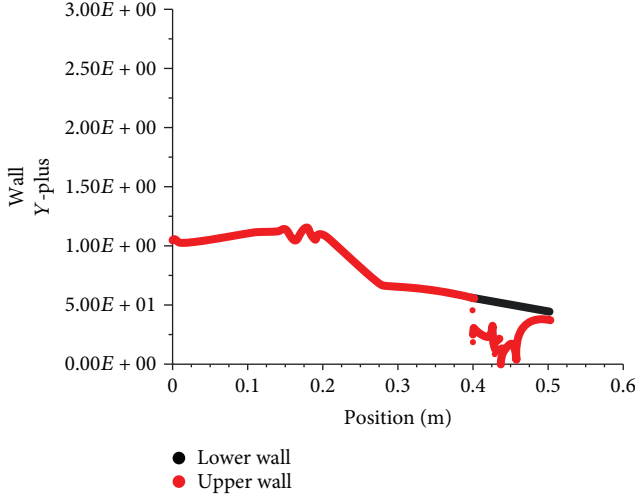
FIGURE 2: Wall Y-plus along the lower and upper walls.

TABLE 1: Computational grids for grid independence study.

No.	Grid size	Injector grid	Height of the first grid	Wall Y-plus
1	300×690	40×75	0.000508 mm	0.45-1
2	200×640	40×75	0.000508 mm	0.45-1
3	150×400	30×75	0.000508 mm	0.84-1

the CFL number increased to 1 to speed up the convergence, and the underrelaxation factor remains at 0.25 to ensure the solution stability. For material type, air (ideal gas) was used in all the cases.

In this specific problem, the injection of sonic jet into supersonic flow is inherently turbulent [24, 34]. Thus, the selection of the turbulence model was critical for the solution accuracy. In this study, the experimental data of Gushe [17] were used in the turbulence model validation.

The realizable $k - \varepsilon$ model, $k - \omega$ model, and shear stress transport (SST) $k - \omega$ model were used in the validation against the experimental data.

The two transport equations for the realizable $k - \varepsilon$ model are [35]

$$
\begin{aligned}
\frac{\partial}{\partial t}(\rho k) + \frac{\partial}{\partial x_j}(\rho k u_j) &= \frac{\partial}{\partial x_j}\left[\left(\mu + \frac{\mu_t}{\sigma_k}\right)\frac{\partial k}{\partial x_j}\right] \\
&\quad + G_k + G_b - \rho \epsilon - Y_M, \\
\frac{\partial}{\partial t}(\rho \varepsilon) + \frac{\partial}{\partial x_j}(\rho \varepsilon u_j) &= \frac{\partial}{\partial x_j}\left[\left(\mu + \frac{\mu_t}{\sigma_\varepsilon}\right)\frac{\partial \varepsilon}{\partial x_j}\right] + \rho C_1 S\varepsilon \\
&\quad - \rho C_2 \frac{\varepsilon^2}{k + \sqrt{\nu\varepsilon}} + C_{1\varepsilon}\frac{\varepsilon}{k}C_{3\varepsilon}G_b,
\end{aligned}
\tag{1}
$$

where

G_k Generation of turbulence kinetic energy due to mean velocity gradients

G_b Generation of turbulence kinetic energy due to buoyancy

Y_M Contribution of the fluctuating dilatation in compressible turbulence to the overall dissipation rate

C_1 and C_2 Constants

σ_k and σ_ε Turbulent Prandtl number for k and ϵ.

The two transport equations for the $k - \omega$ model are [35]

$$
\begin{aligned}
\frac{\partial}{\partial t}(\rho k) + \frac{\partial}{\partial x_i}(\rho k u_i) &= \frac{\partial}{\partial x_j}\left(\Gamma_k \frac{\partial k}{\partial x_j}\right) + G_k - Y_k + S_k, \\
\frac{\partial}{\partial t}(\rho \omega) + \frac{\partial}{\partial x_i}(\rho \omega u_i) &= \frac{\partial}{\partial x_j}\left(\Gamma_\omega \frac{\partial \omega}{\partial x_j}\right) + G_\omega - Y_\omega + S_\omega,
\end{aligned}
\tag{2}
$$

where

G_k Generation of turbulence kinetic energy due to mean velocity gradients

G_ω Generation of ω

Y_k and Y_ω Dissipation of k and ω due to turbulence

Γ_k and Γ_ω Dissipation of k and ω due to turbulence

The two transport equations for the shear stress transport (SST) $k - \omega$ model are [35–37]

$$
\begin{aligned}
\frac{\partial}{\partial t}(\rho k) + \frac{\partial}{\partial x_i}(\rho k u_i) &= \frac{\partial}{\partial x_j}\left(\Gamma_k \frac{\partial k}{\partial x_j}\right) + \widetilde{G_k} - Y_k + S_k, \\
\frac{\partial}{\partial t}(\rho \omega) + \frac{\partial}{\partial x_i}(\rho \omega u_i) &= \frac{\partial}{\partial x_j}\left(\Gamma_\omega \frac{\partial \omega}{\partial x_j}\right) + G_\omega - Y_\omega + D_\omega + S_\omega,
\end{aligned}
\tag{3}
$$

where

$\widetilde{G_k}$ Generation of turbulence kinetic energy due to mean velocity gradients

G_ω Generation of ω

Y_k and Y_ω Dissipation of k and ω due to turbulence

Γ_k and Γ_ω Dissipation of k and ω due to turbulence

D_ω Effective diffusivity of k and ω

The wall Y-plus about 1 in the boundary layer was achieved as shown in Figure 2; for this purpose, the first cell height in the nozzle wall is predicted by using the skin friction coefficient (C_f) for the flat plate.

$$
C_f = 0.0576\left(\text{Re}_{x)}\right)^{-0.2},
\tag{4}
$$

where the suffix $\{x\}$ is related to the distance in which the boundary layer separation occurs and it is calculated from the inlet of the nozzle to the point of injection, and utilizing the wall Y-plus and $U\tau$ equations, the first cell height is predicted. Then by numerical simulation, it was validated.

A typical structured grid system is selected to be utilized in the computational domain for grid independence analysis. Table 1 shows the three grids with different aspects used for the independence analysis.

Upon grid independence analysis, the primary axial thrust was almost identical for the three grids; the maximum difference between the three grids for this value was less than 0.5%. As a result, in order to achieve more accuracy in the
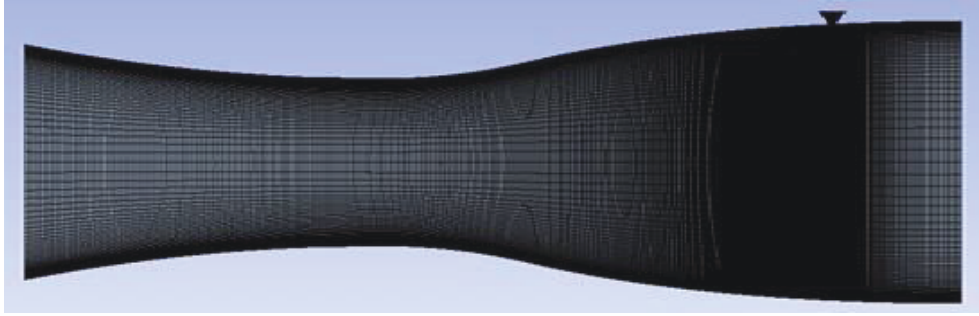
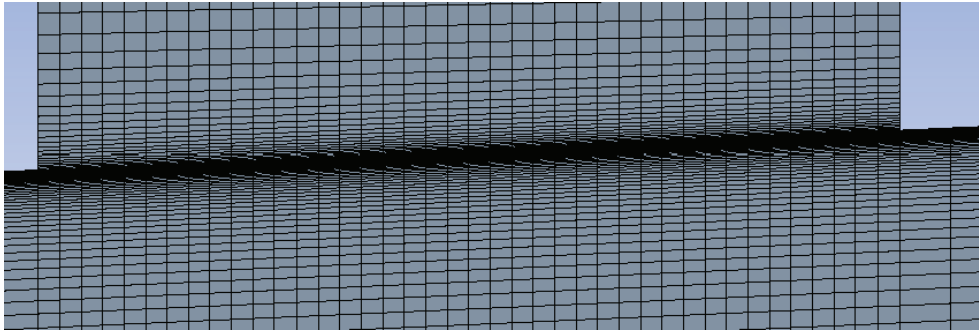FIGURE 3: Computational structured grid 2.

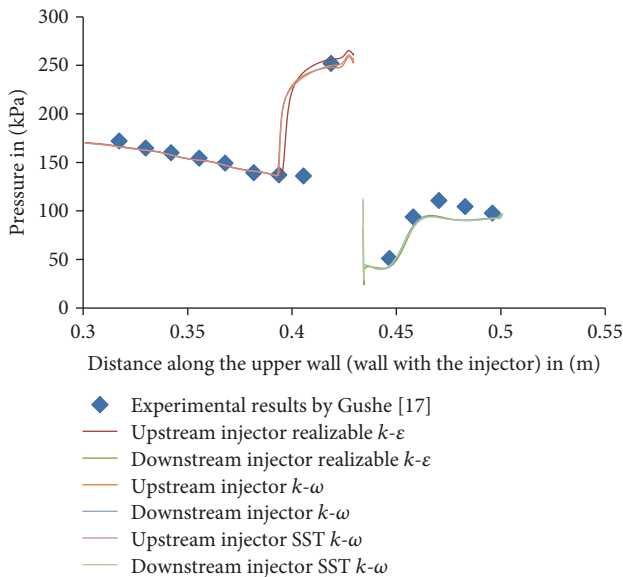FIGURE 4: Near view at the injection slot in grid 2.

FIGURE 5: Comparison between numerical results and experimental data for static pressure distribution upstream and downstream the injector along the upper wall using different turbulence models.

numerical simulation, grid 2 was selected for the turbulence model validation study. In the computational grid 2 shown in Figure 3, the mesh near upstream, downstream the injection slot and the nozzle walls were refined carefully as shown in Figure 4.

Static pressure distribution along the upper wall (with injector) and the lower wall (without injector) was used for the comparison between the numerical results and

experimental data by Gushe [17]. The realizable $k - \varepsilon$ model, $k - \omega$ model, and shear stress transport (SST) $k - \omega$ model were used in the comparison.

Figure 5 shows that the three models behave similarly, having an excellent accuracy in the unaffected zone and good accuracy with error than less 10% in the high- and low-pressure zones compared to the experimental data; also for the boundary layer separation point, there is little difference (slightly overpredicted) between the numerical results and experimental data.

Figure 6 shows that all the models behave in an excellent accuracy with the experimental data. Finally, the three turbulence models behave similarly, so the realizable $k - \varepsilon$ turbulence model with enhanced wall treatment was selected, as it is advised for flows containing a boundary layer under strong adverse pressure gradients [35], and it converges faster than the other two models do, whereas the $k - \omega$ model and the shear stress transport (SST) $k - \omega$ model take about 8 hours (about 35000 iterations) to converge, while the realizable $k - \varepsilon$ model takes about 6 hours (about 25000 iterations) for convergence, so the calculation time can be reduced.

Also, in order to verify the current model, the amplification factor calculated by Gushe [17] compared to amplification factor calculated from the numerical simulation shows good accuracy.

After validating and choosing the turbulence model, the solution of the two-dimensional flow field in a conical convergent divergent nozzle with SITVC has been carried out. The injector used for the secondary injection was a two-dimensional slot extended throughout the depth of the primary nozzle in the z-axis with different injection locations M_p (in terms of axial Mach number of primary flow
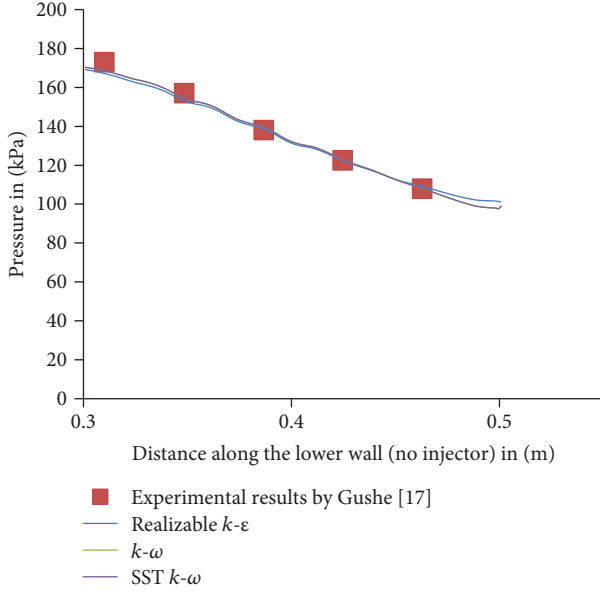
FIGURE 6: Comparison between numerical results and experimental data for static pressure distribution along the lower wall using different turbulence models.

corresponding to the injection point located on the primary nozzle wall) = 2, 2.5, and 2.75; injection angles 45°, 80°, 90°, 100°, and 135° as in Figure 7 (when the secondary injection is in the direction of the primary flow, the injection angle is 0°); and primary nozzle divergence half angles 5°, 10°, and 15°; the geometric model of the two-dimensional convergent divergent nozzle used in the numerical investigation is shown in Figure 7.

Also, for a grid independence analysis, a typical structured grid system has been utilized in the computational domain as shown in Table 2.

The grid independence analysis results showed that the primary axial thrust was almost identical and the maximum difference between the three grids for this value was less than 0.2%. Based on the grid independence study, grid 2 was used for more accuracy and lower computational time.

The computational structured grid 2 is shown in Figure 8; the mesh refined around the injection slot and the nozzle walls is shown in Figure 9 to achieve a wall Y-plus about 2 at the nozzle critical section and less than 1 at the injection slot as shown in Figure 10.

It has been supposed that the numerical solution converged for each case when the mass flow rate monitor at the inlet control volume displays no change (constant watching is kept at a considerable number of digits) with more than 100 sequential iterations [38].

2.1. Boundary Conditions.
A pressure inlet boundary was chosen for inlet and outlet of the primary nozzle, and the mass flow inlet boundary was used for the secondary inlet.

Inlet: primary stagnation pressure P_{op} = 3720 kPa, primary stagnation temperature T_{op} = 300 K

Outlet: primary nozzle exit pressure, P_{ep} = 101.325 kPa, exit Mach number = 3

Secondary inlet: mass flow rate = 4.34255 kg/s, secondary to primary mass flow rate $\dot{m}_s/\dot{m}_P$ = 2.54%, secondary to primary stagnation pressure ratio P_{os}/P_{op} = 0.5, secondary injection temperature T_{os} = 300 K, and ratio between secondary injection slot area and primary critical area A_s/A^* = 0.05

2.2. SITVC Performance Parameters.
SITVC performance parameters investigated in the current study include [13, 39]

(1) Axial thrust augmentation ATA%

$$\text{ATA}\% = \frac{F_P - F_P^o}{F_P}. \tag{5}$$

(2) Thrust ratio: the ratio between the side force and the axial thrust force F_s/F_P where

(i) Side force F_s

$$F_s = F_i + F_j, \tag{6}$$

F_i is the interaction force (side force-pressure component).

$$F_i = \sum_i \left[P \Delta A_y \right]_{\text{upper wall}} - \sum_i \left[P \Delta A_y \right]_{\text{lower wall}}, \tag{7}$$

where i means that the summation is taken over all the cells of the computational grid

F_j is the jet reaction force (side force-momentum component).

$$F_j = \dot{m}_s V_{sy} + \left((P_{es} - P_{as}) A_s \right) \cos \beta_{\text{inj}}. \tag{8}$$

(ii) Primary axial thrust F_P:

$$F_P = \dot{m}_e V_x + (P_e - P_a) A_e. \tag{9}$$

(3) System-specific impulse loss δIsp

$$\delta Isp = Ispsys - Isp^\circ. \tag{10}$$

(4) Specific impulse ratio (amplification factor) AK is the ratio of the secondary injection-specific impulse to the primary flow-specific impulse, and it determines the amount of secondary fluid to be injected to achieve a specified side force [10].
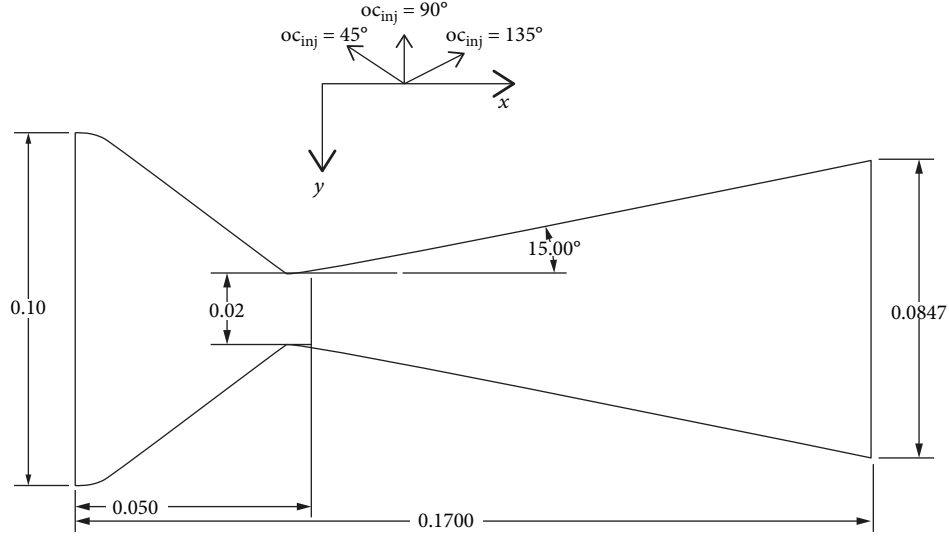
$$\text{AK} = \frac{Isps}{Isp^\circ}, \tag{11}$$

FIGURE 7: Geometric model of 2D convergent divergent nozzle (units in m).

TABLE 2: Computational grids for the grid independence study.

No.	Grid size	Injector grid	Height of first grid	Wall Y-plus
1	200×300	40×75	0.0004 mm	0.45-1.77
2	240×400	10×70	0.0004 mm	0.45-2
3	300×500	15×70	0.0004 mm	0.84-2.6

where

$$Isp° = \frac{F_P^o}{\dot{m}_P \times g},$$

$$Isps = \frac{F_s}{\dot{m}_s \times g}, \qquad (12)$$

$$Ispsys = \frac{\sqrt{F_P^2 + F_s^2}}{(\dot{m}_s + \dot{m}_P)g}.$$

3. Results and Discussion

3.1. Flow Field Structure. For a constant secondary mass flow rate influence of the injection location, the injection angle and primary nozzle divergence half angle on the nozzle flow field structure will be discussed in the following part.

3.1.1. Components of the Flow Field Structure. The SITVC creates a complex flow field in the nozzle divergent part; Figure 11 illustrates the main components of the SITVC flow field.

3.1.2. Influence of Injection Location. For a given secondary mass flow rate and injection angle, the change in the flow field structure as a function of injection location will be investigated in this part. The strength of the primary bow shock decreases as the injection location moved farther downstream due to the increase in the primary flow Mach number decreasing the angle of the primary bow shock also in case of

downstream injection $M_P = 2.75$; the relatively shorter wall length available on the opposite wall for shock impact minimizes the possibility of shock impingement as it can be seen in Figure 12.

The momentum flux ratio J is an important parameter in determining the separation distance and the depth of penetration of a jet in cross flow as in eqn. (13) [11, 29]. J increases as the injection location moves downstream, as shown in Table 3, leading to increasing penetration depth and the separation distance upstream the injection

$$J = \frac{\rho_j V_j^2}{\rho_\infty V_\infty^2} = \frac{\gamma_j P_j M_j^2}{\gamma_\infty P_\infty M_\infty^2}. \qquad (13)$$

As well, the injection location moving downstream the boundary layer is more developed which decreases the slope of velocity gradient (du/dy) and increases the possibility of boundary layer separation [40, 41] as it can be observed in Figure 13.

It was noticed that the strength of the separation decreases as the injection location goes downstream; this is due to increase in the primary flow Mach number decreasing the separation shock angle, and this in turn results into a relatively lower pressure in the upstream higher pressure zone. Downstream the injector, the lower pressure zone expands, as the injection location moved farther downstream, as shown in Figure 13.

The chance of shock impingement is very high in case of upstream injection $M_P = 2$ but only if the secondary mass flow rate was small, and as the injection location moved farther downstream $M_P = 2.5$ and 2.7, the chance of the primary bow shock impingement decreases, as shown in Figure 14. Finally, as the injection location moved downstream, the interaction force increases by increasing the primary flow velocity and the jet reaction force increases by decreasing the primary flow pressure.
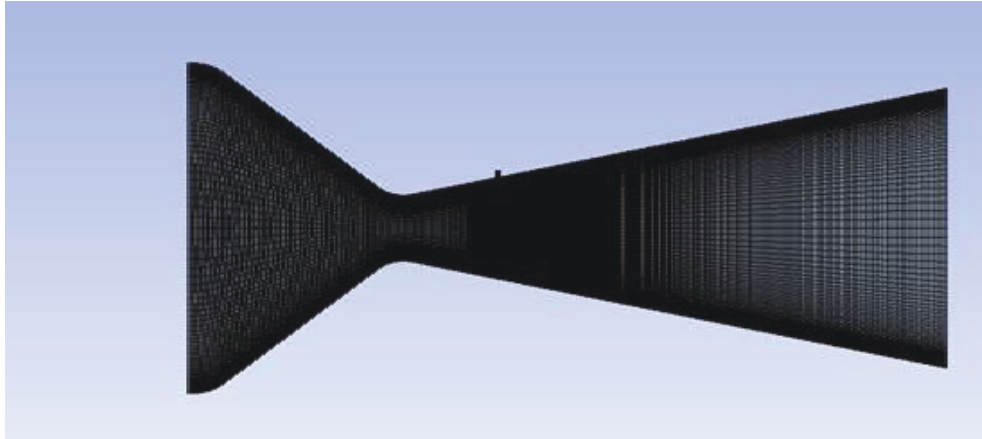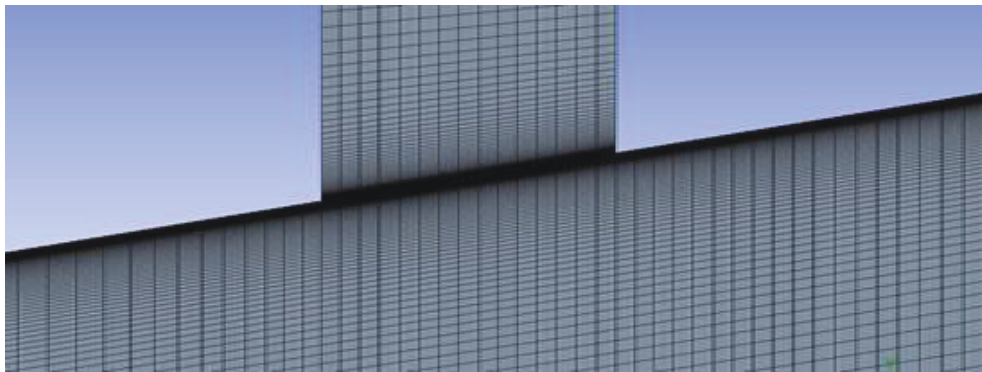
FIGURE 8: Computational structured grid 2.

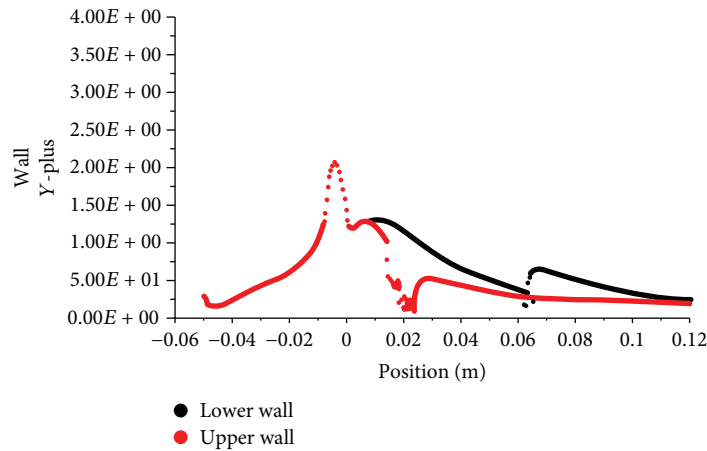
FIGURE 9: Near view at the injection slot grid 2.

FIGURE 10: Wall Y-plus along lower and upper walls for grid 2.

3.1.3. Influence of Injection Angle. For a given secondary mass flow rate and injection location, the influence of the injection angle will be investigated in this section. The momentum of the secondary injection decreases as the injection angle inclined downstream or upstream, so the momentum flux J decreases as shown in Table 4, but in the case of upstream inclination due to the existence of the portion of the injection in the upstream region, the interaction increases as it appears as an additional "block" that pushes the separated boundary layer leading to an increase in the separation as shown in Figure 15(c). As a result of the previous reason, as the angle of injection is increased (towards perpendicular or upstream inclination), the strength of primary bow shock increases and its originating point moves upstream the injector, and the strength of separation increases as the angle of injection increases (upstream inclination) which leads to an extension
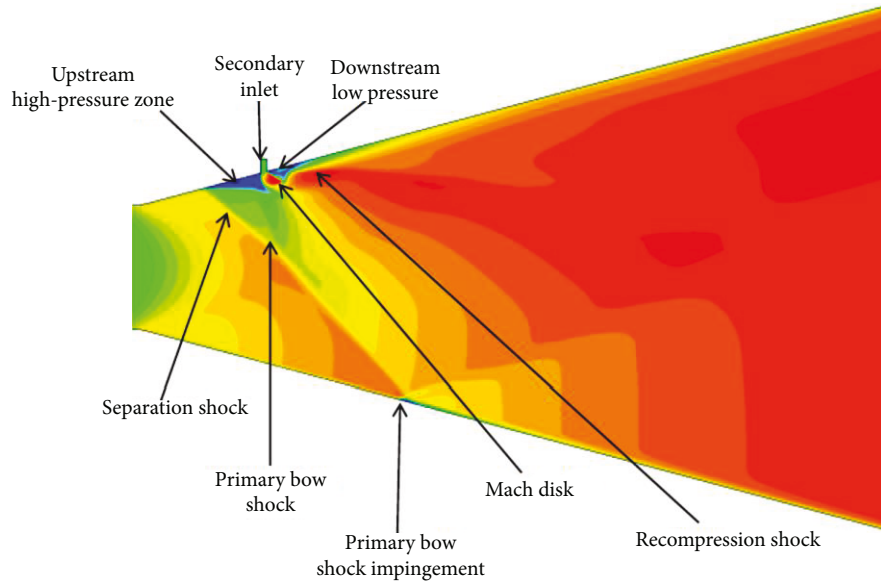
FIGURE 11: SITVC nozzle flow field structure (Mach number contour).

(a) $M_p = 2$
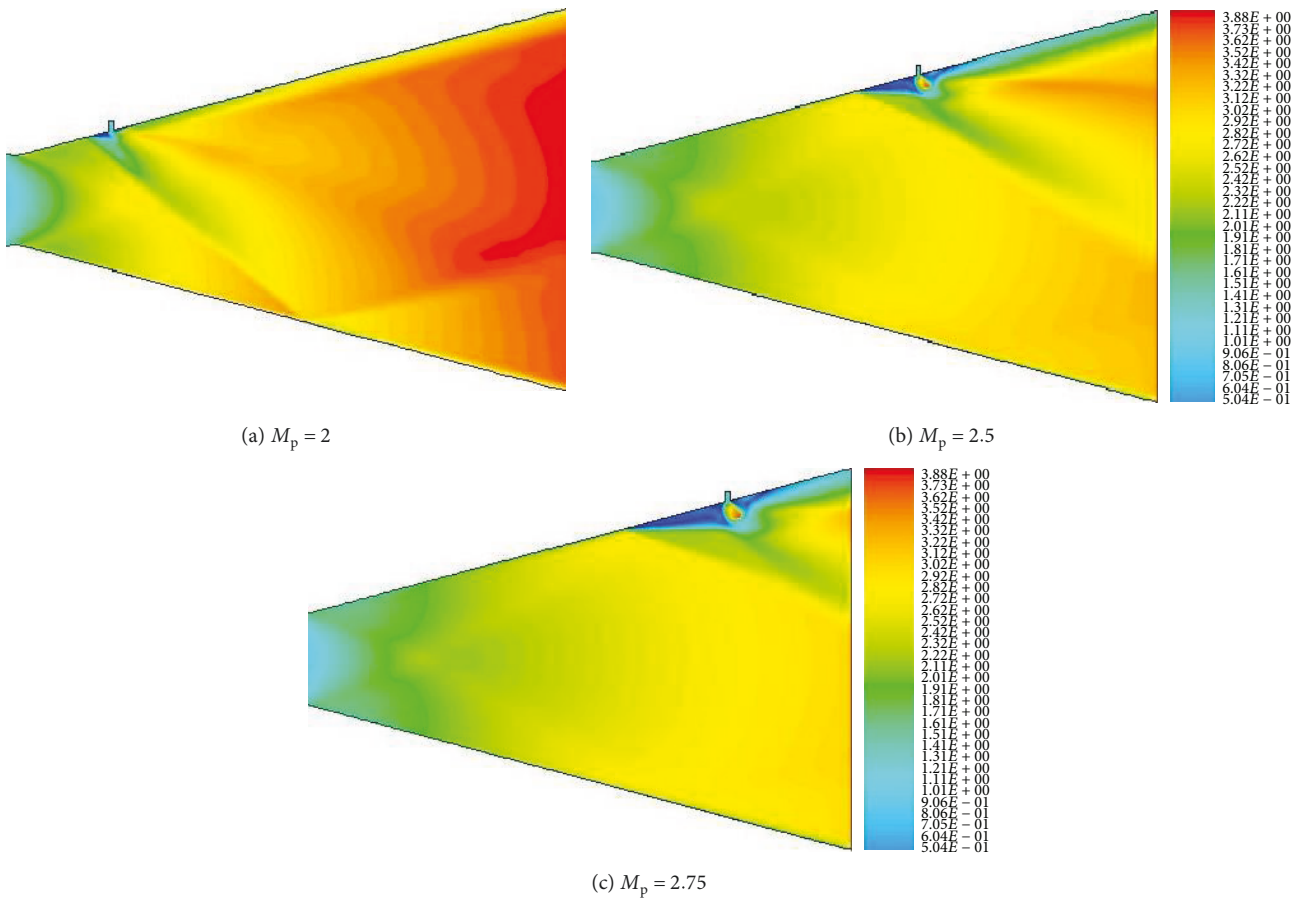
(b) $M_p = 2.5$

(c) $M_p = 2.75$

FIGURE 12: The influence of injection location on flow field structure (Mach number contour).

of the higher-pressure zone upstream the injector; thus, a stronger separation shock results in higher pressure in the high-pressure zone upstream the injector as shown in

Figures 15 and 16. Also, the strength of primary bow shock decreases as the injection angle decreases (downstream inclination) due to the decrease in the momentum flux ratio J, as

TABLE 3: Momentum flux ratio J with injection location.

M_p	J
2	0.45
2.5	0.7
2.75	0.85

TABLE 4: Momentum flux ratio J with injection angle at $M_p = 2.75$.

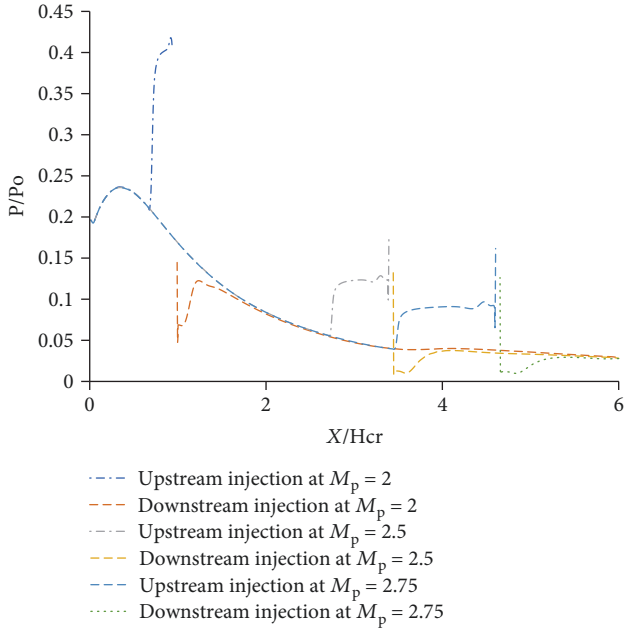| $\propto_{inj}$	J
45°	0.6010
90°	0.85
135°	0.6010

FIGURE 13: Influence of injection location on the static pressure distribution along the injector wall.
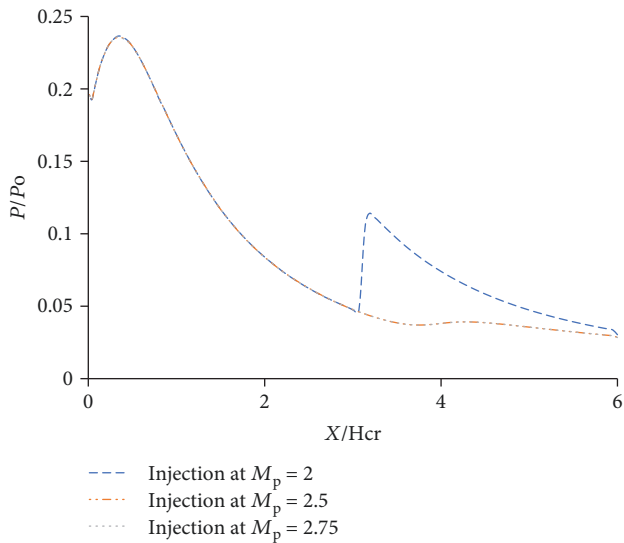

FIGURE 14: Influence of injection location on the static pressure distribution along the lower wall.

shown in Figures 16 and 17. Thus, in case of shock impingement, the downstream injection angles $\propto_{inj} = 45°$ diminish the effect of shock impingement on the opposite wall as shown in Figure 18, and by increasing the injection angle (upstream inclination) to $\propto_{inj} = 135°$, the chance of primary bow shock impingement on the opposite wall increases, and the impact point of the shock moves further upstream on the opposite wall with the increase in the angle of injection (upstream inclination). Injection at upstream angles of injection produces a stronger shock impact as it can be observed in Figure 18.

3.1.4. Influence of Primary Nozzle Divergence Half Angle

(1) At Injection Location $M_p = 2$. For a given secondary mass flow rate, the strength of the primary bow shock increases by decreasing the divergence half angle, as the rate of increase in Mach number contour is lower due to the greater wall length with the same expansion ratio.

Momentum flux ratio J decreased in smaller divergence half angles as in Table 5, due to an increase in the velocity of the primary nozzle flow (decreasing cosine effect), but a smaller divergence half angle results in a slight expansion of the pressure zones upstream and downstream the injector as depicted in Figure 19, as a result of the development of the boundary layer and lower pressure contour upstream the injector (the rate of decrease in the pressure contour is lower). The strength of the recompression shock increases, as the divergence half angle decreases; in the 5° divergence half angle, the recompression shock increases till it reaches the lower wall and is reflected as can be observed in Figure 20. It can be observed that the shock impingement increases and moves downstream as the divergence half angle decreases as in Figure 21; furthermore, upstream injection accompanied with smaller divergence half angles results into multiple primary bow shock impingement on the lower and upper walls due to the increase in shock impingement on the lower wall and reflected to the upper wall as shown in Figures 19–21.

(2) At Injection Location $M_p = 2.75$. For a given secondary mass flow rate, the strength of the primary bow shock increases by the decrease in the divergence half angle; also, the secondary bow shock increases by the decrease in the divergence half angle as shown in Figure 22. Although J is more in the higher divergence half angles as in Table 6, due to the lower rate of decrease in the pressure contour in smaller divergence half angles and the more developed boundary layer, the separation distance in the upstream high-pressure zone is almost identical as shown in Figure 23. Smaller divergence half angles extend the lower pressure zone as depicted in Figure 23. For a given secondary mass flow rate, injection

(a) $\alpha_{inj} = 45°$

(b) $\alpha_{inj} = 90$

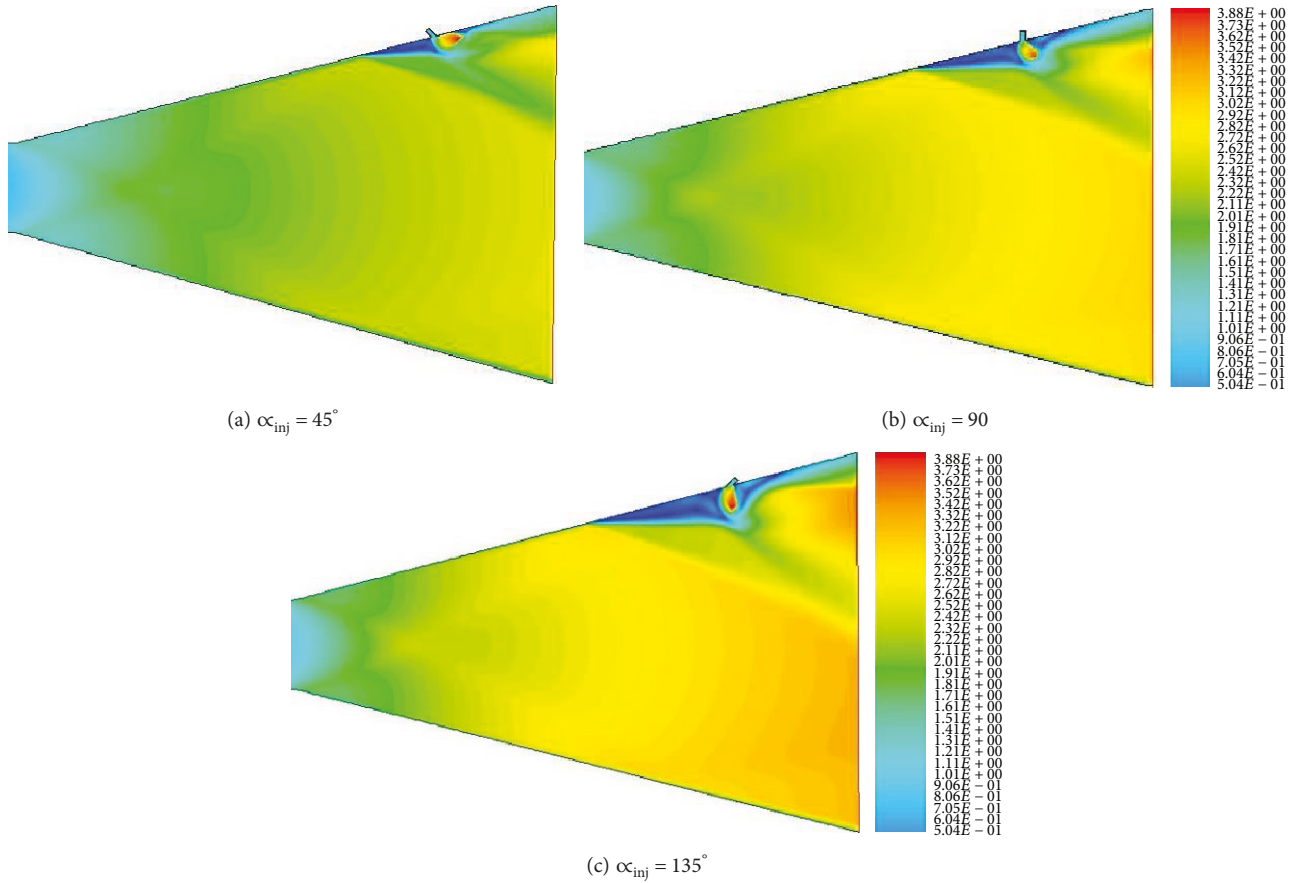(c) $\alpha_{inj} = 135°$

FIGURE 15: The influence of injection angle on flow field structure (Mach number contour) $M_p = 2.75$.
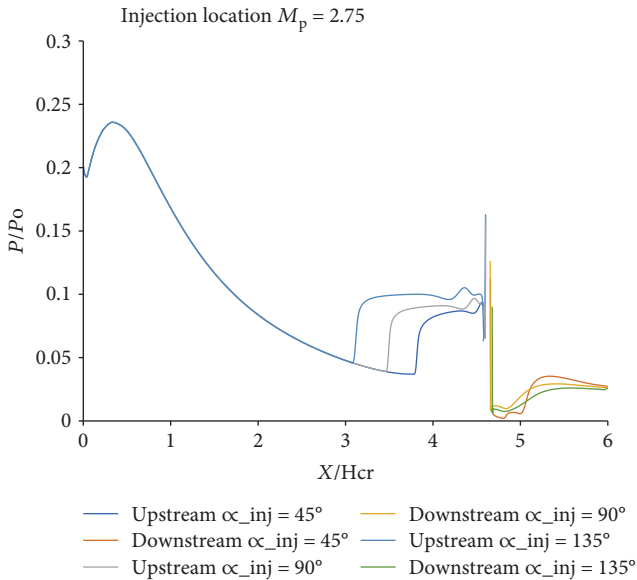

FIGURE 16: Influence of the injection angle on the static pressure distribution along the injector wall $M_p = 2.75$.

location downstream injection with smaller divergence half angle results into no shock impingement as can be observed in Figure 22.

3.2. Performance Analysis. SITVC performance was investigated for injection location, angle of injection, and primary nozzle divergence half angle for the same secondary mass flow rate for all cases.

3.2.1. Influence of Injection Location. For a given secondary mass flow rate, it was observed as shown in Table 7 that upstream injection increases the axial thrust augmentation; this is due to the efficient adiabatic expansion of the injected gases. The amplification factor increases as the injection location moved downstream as the chance of shock impingement decreases; also, the thrust ratio increases as the injection location moved downstream due to the increase in the side force. The system-specific impulse loss increases as the injection location moved farther downstream due to inefficient adiabatic expansion and the increase in the side force.

3.2.2. Influence of Injection Angle. The given secondary mass flow rate and injection location are shown in Tables 8 and 9. The axial thrust augmentation increases as the injection angle decreases to 45°; this is due to the relatively higher parallel velocity (to nozzle axis) component of the injection gas. The thrust ratio increases (negative due to shock impingement or positive no impingement) by the increase in the injection angle as the side force increases (negative or positive); as the injection angle increases to 135°, the rate of increase in interaction force is more than the rate of decrease
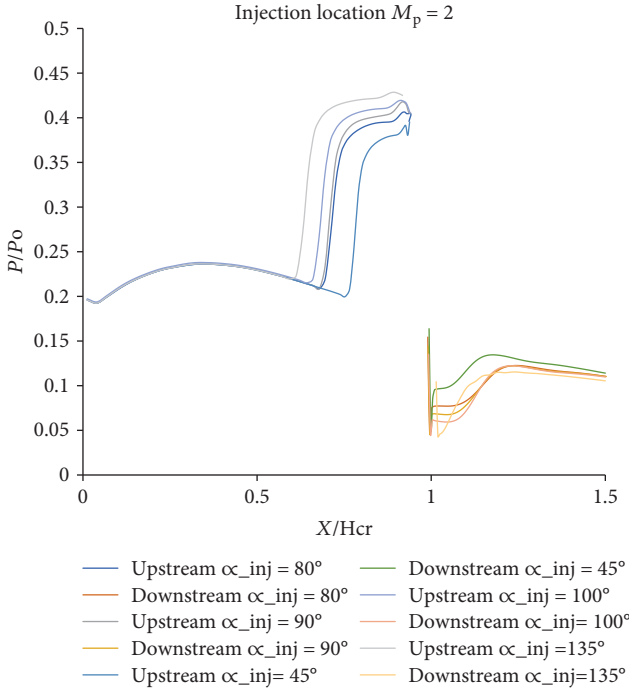
FIGURE 17: Influence of the injection angle on the static pressure distribution along the injector wall $M_p = 2$.
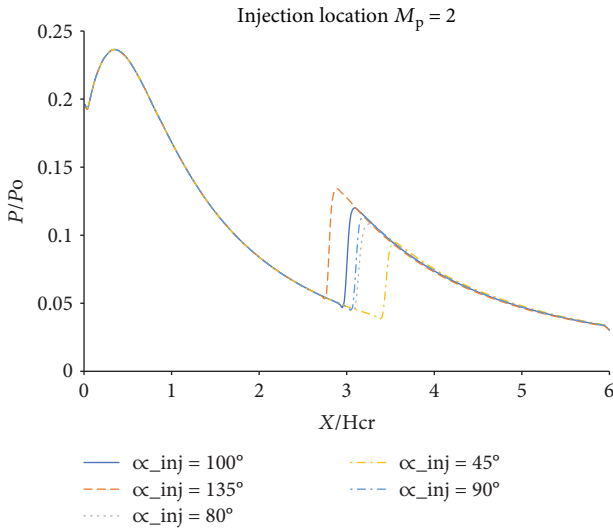

FIGURE 18: Influence of the injection angle on the static pressure distribution along the lower wall $M_p = 2$.

TABLE 5: Momentum flux ratio J with divergence half angle at $M_p = 2$.

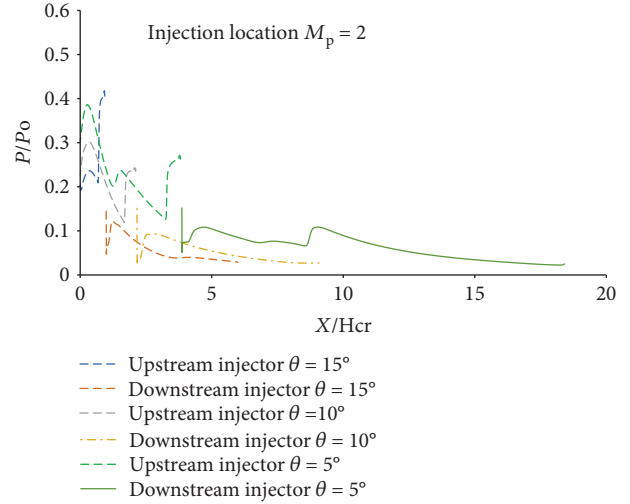| θ	J
5°	0.4363
10°	0.441
15°	0.45

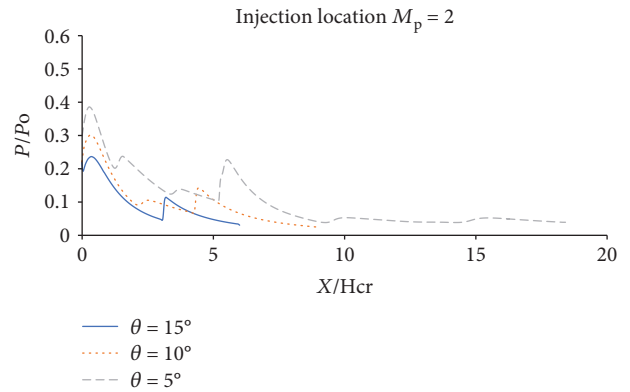FIGURE 19: Influence of the divergence half angle on injector wall static pressure distribution $M_p = 2$.

FIGURE 20: Influence of the divergence half angle on lower wall static pressure distribution $M_p = 2$.

in the jet reaction force (due to the inclination). The amplification factor and specific impulse loss increases (negative in case of shock impingement or positive) as the injection angle increases to 135°.

3.2.3. Influence of Primary Nozzle Divergence Half Angle. For a given secondary mass flow rate, the upstream injection $M_p = 2$ is as shown in Table 10 and the downstream injection $M_p = 2.75$ is as shown in Table 11; the axial thrust augmentation increases by the increase in the divergence

angle, but the system-specific impulse loss increases by the decrease in the divergence half angle due to a decrease in the primary axial thrust. The thrust ratio and amplification factor increase by the increase in the divergence half angle due to the increase in the side force as a result of the increase in the value of the interaction force; this is at the downstream injection, but at the upstream injection, this changes due to the increase in shock impingement in the 10° divergence half angle and the multiple shock impingements in case of the 5° divergence half angle.
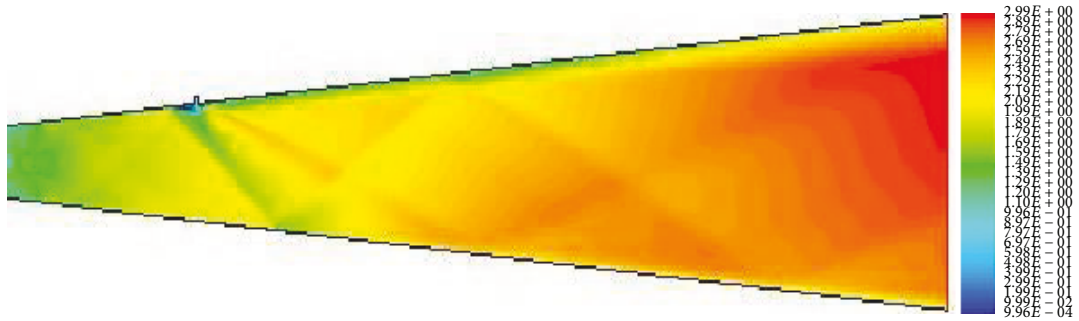
(a) Div-half angle $\theta = 5°$
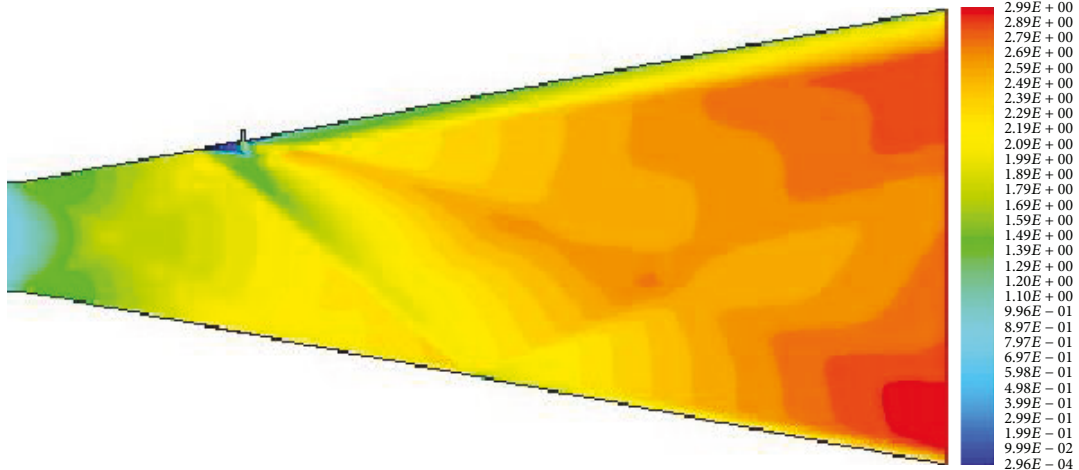
(b) Div-half angle $\theta = 10°$
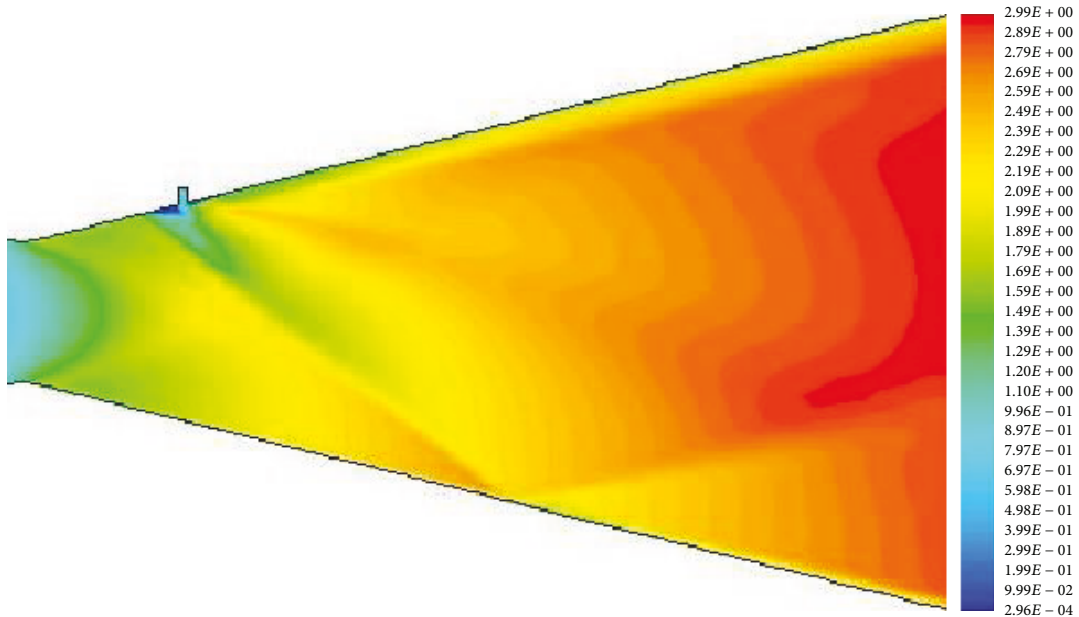
(c) Div-half angle $\theta = 15°$

Figure 21: The influence of primary nozzle divergence half angle on flow field structure (Mach number contour) $M_p = 2$.

4. Conclusions

Numerical simulation has been carried out with the help of the realizable $k - \varepsilon$ turbulence model accompanied with enhanced wall treatment and showed a good accuracy with the experimental data in order to analyze the influence of changing the injection angle, injection location, and primary nozzle divergence half angle on the SITVC nozzle flow field
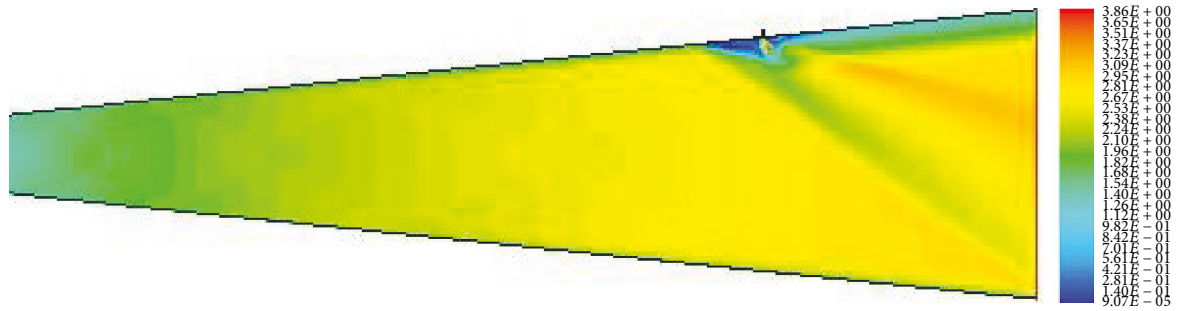
(a) Div-half angle $\theta = 5°$
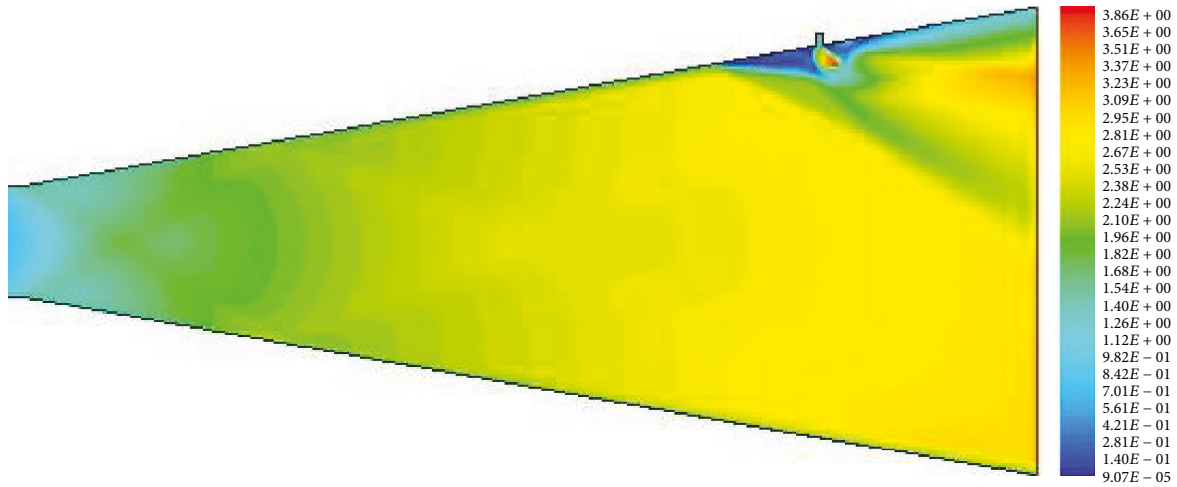
(b) Div-half angle $\theta = 10°$
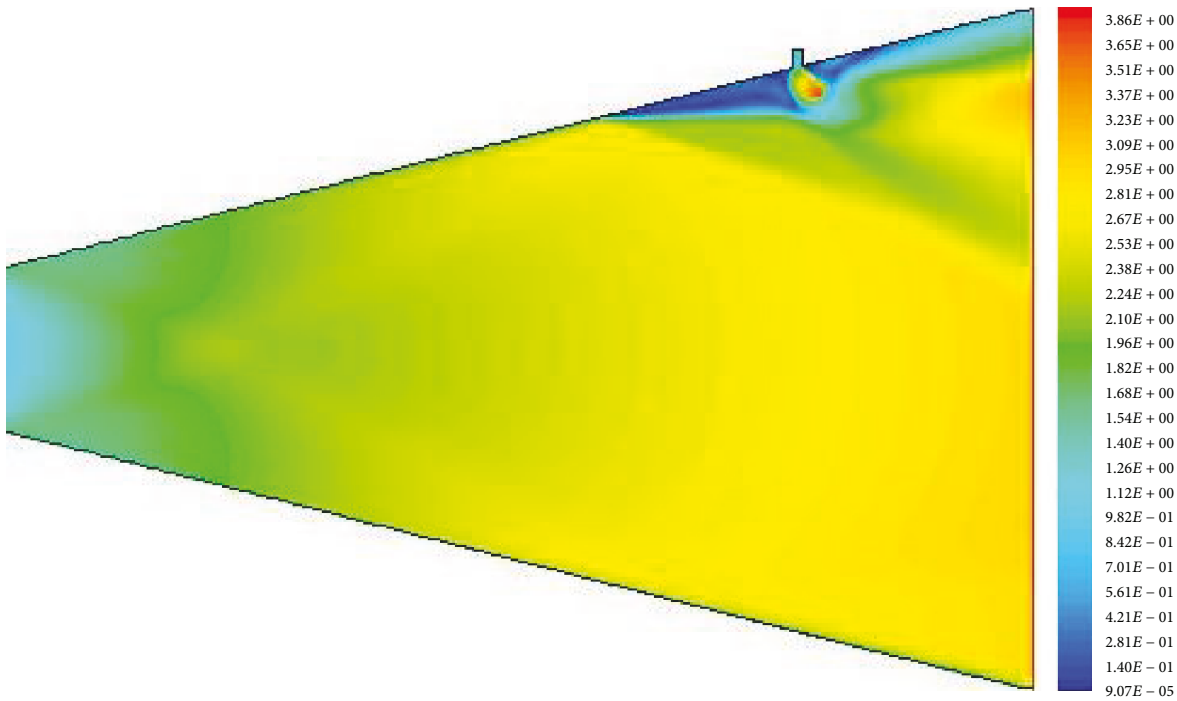
(c) Div-half angle $\theta = 15°$

FIGURE 22: The influence of primary nozzle divergence angle on flow field structure (Mach number contour) $M_\mathrm{p} = 2.75$.

structure and the SITVC performance parameters for a given secondary mass flow rate. It was found that as the injection location moved downstream $M_\mathrm{p} = 2.75$, the chance of shock impingement decreases and the side force increases, but the axial thrust augmentation decreases due to the inefficient expansion of the secondary injection, also with increasing

TABLE 6: Momentum flux ratio J with divergence half angle at $M_p = 2.75$.

θ	J
5°	0.824
10°	0.8337
15°	0.85

FIGURE 23: Influence of the divergence half angle on injector wall static pressure distribution $M_p = 2.75$.

TABLE 7: SITVC performance parameters with respect to injection location.

	ATA%	AK	$F_s/F_P\%$	δIsp
$M_p = 2$	2.354	-0.95	-2.36	-0.09203
$M_p = 2.5$	0.983	1.7247	4.34	-0.8958
$M_p = 2.75$	1.132	1.95	4.9	-0.7815

TABLE 8: SITVC performance parameters with respect to the injection angle at $M_p = 2.75$.

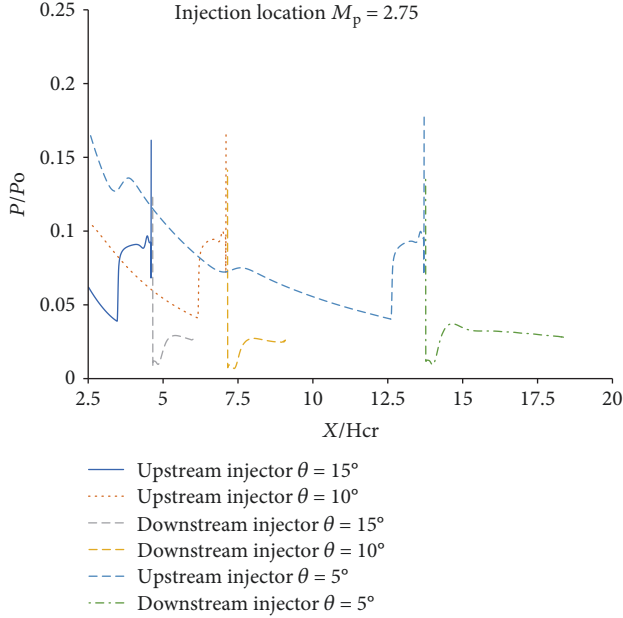|	ATA%	AK	$F_s/F_P\%$	δIsp
$\alpha_{inj} = 45°$	2.429	-0.73	-1.829	-0.0541
$\alpha_{inj} = 80°$	2.365	-0.945	-2.3508	-0.08624
$\alpha_{inj} = 90°$	2.354	-0.9524	-2.37	-0.092033
$\alpha_{inj} = 100°$	2.28	-1.11733	-2.78	-0.1318
$\alpha_{inj} = 135°$	2.1343	-1.59	-3.97	-0.19

α_{inj} from 45° to 135°; the side force increases, but axial thrust augmentation slightly decreases, and it was concluded that small divergence half angles 5° are not efficient from the point of view of SITVC as the chance of the shock impingement increases. Finally, results showed that downstream injection,

TABLE 9: SITVC performance parameters with respect to the injection angle at $M_p = 2.75$.

	ATA%	AK	$F_s/F_P\%$	δIsp
$\alpha_{inj} = 45°$	1.2	1.7	4.2	-0.513
$\alpha_{inj} = 90°$	1.132	1.95	4.9	-0.7815
$\alpha_{inj} = 135°$	1.03	2.21	5.5	-1.121

TABLE 10: SITVC performance parameters with respect to divergence half angle at $M_p = 2$.

	ATA%	AK	$F_s/F_P\%$	δIsp
$\theta = 5°$	1.723	-0.9524	-0.5	-0.45
$\theta = 10°$	1.84	-1.4270	-3.5	-0.382
$\theta = 15°$	2.35	-0.2118	-2.36	-0.0920

TABLE 11: SITVC performance parameters with respect to divergence half angle at $M_p = 2.75$.

	ATA%	AK	$F_s/F_P\%$	δIsp
$\theta = 5°$	0.4	1.798	4.55	-1.123
$\theta = 10°$	0.68	1.86634	4.7	-1.05
$\theta = 15°$	1.13	1.949	4.9	-0.7815

increasing the injection angle (towards upstream inclination) and higher divergence half angle, improves the performance of SITVC.

Nomenclature

A_s: Secondary injection area (m^2)
F_p^0: Primary axial thrust without injection (N)
Hcr: Nozzle throat height
M_p: Injection location (in terms of axial Mach number of primary flow corresponding to the injection point located on the primary nozzle wall)
$\dot{m}_e$: Total exit mass flow rate (kg/s)
$\dot{m}_p$: Primary mass flow rate (kg/s)
$\dot{m}_s$: Secondary mass flow rate (kg/s)
P: Pressure (Pa)
P_{es}: Secondary exit pressure (Pa)
P_{as}: Ambient pressure at the secondary port before injection (Pa)
Re_x: Reynolds number at the distance x
$U\tau$: Friction velocity (m/s)
V_x: Velocity along the x-axis (m/s)
V_{sy}: Secondary gas velocity along the y-direction (m/s)
X: Distance along the nozzle wall
Isp_s: Secondary specific impulse (sec)
$Ispsys$: System-specific impulse (sec)
Isp_p^o: Primary specific impulse without injection (sec)
δIsp: System-specific impulse loss
θ: Divergence half angle (deg)
α_{inj}: Injection angle (deg)
β_{inj}: Wall angle at point of injection (deg)
γ: Specific heat ratio.

Data Availability

The data used to support the findings of this study are available from the corresponding author upon request.

Conflicts of Interest

The authors declare that there is no conflict of interests regarding the publication of this paper.

References

[1] G. P. Sutton and O. Biblarz, *Rocket Propulsion Elements*, John Wiley & Sons, 7 edition, 2001.

[2] S. Vignesh, N. Vishnu, S. Vigneshwaran, M. Vishnu Anand, D. K. Babu, and V. R. Sanal Kumar, "Numerical studies on thrust vectoring using shock-induced self impinging secondary jets," *International Journal of Mechanical, Aerospace, Industrial, Mechatronic and Manufacturing Engineering*, vol. 9, no. 6, pp. 1118–1124, 2015.

[3] D. J. Wing and V. J. Giuliano, "Fluidic thrust vectoring of an axisymmetric exhaust nozzle at static conditions," Tech. Rep. FEDSM97-3228, ASME, 1997.

[4] K. A. Deere, "Summary of fluidic thrust vectoring research at NASA Langley research center," in *21st AIAA Applied Aerodynamics Conference*, pp. 1–18, Orlando, FL, USA, 2003, AIAA 2003-3803.

[5] M. Sellam, V. Zmijanovic, L. Leger, and A. Chpoun, "Assessment of gas thermodynamic characteristics on fluidic thrust vectoring performance: analytical, experimental and numerical study," *International Journal of Heat and Fluid Flow*, vol. 53, pp. 156–166, 2015.

[6] S. Jain, S. Roy, D. Gupta, V. Kumar, and N. Kumar, "Study on fluidic thrust vectoring techniques for application in V/STOL aircrafts," SAE Technical Paper 2015-01-2423, SAE International, 2015.

[7] R. Balu, A. G. Marathe, P. J. Paul, and H. S. Mukunda, "Analysis of performance of a hot gas injection thrust vector control system," *Journal of Propulsion and Power*, vol. 7, no. 4, pp. 580–585, 1991.

[8] J. F. Newton Jr. and F. M. Spaid, "Interaction of secondary injectants and rocket exhaust for thrust vector control," *ARS Journal*, vol. 32, no. 8, pp. 1203–1211, 1962.

[9] J. E. Broadwell, "Analysis of the fluid mechanics of secondary injection for thrust vector control," *AIAA Journal*, vol. 1, no. 5, pp. 1067–1075, 1963.

[10] E. Erdem, K. Albayrak, and H. T. Tinaztepe, "Parametric study of secondary gas injection into a conical rocket nozzle for thrust vectoring," in *42nd AIAA/ASME/SAE/ASEE Joint Propulsion Conference & Exhibit*, pp. 1–11, Sacramento, CA, USA, July 2006.

[11] W. Huang, W.-D. Liu, S.-B. Li, Z.-X. Xia, J. Liu, and Z.-G. Wang, "Influences of the turbulence model and the slot width on the transverse slot injection flow field in supersonic flows," *Acta Astronautica*, vol. 73, pp. 1–9, 2012.

[12] F. W. Spaid and E. E. Zukoski, "A study of the interaction of gaseous jets from transverse slots with supersonic external flows," *AIAA Journal*, vol. 6, no. 2, pp. 205–212, 1968.

[13] M. U. Sadiq, *Performance Analysis and Flowfield Characterization of Secondary Injection Thrust Vector Control (SITVC) for A 2DCD Nozzle, [M.S. thesis]*, Faculty of the Viterbi School of Engineering University of Southern California, 2007.

[14] M. Shandor and R. E. Walker, "Influence of injectant properties for fluid injection thrust vector control," *Journal of Spacecraft and Rockets*, vol. 1, no. 4, pp. 409–413, 1964.

[15] J. M. Wu, R. L. Chapkis, and A. Mager, "Approximate analysis of thrust vector control by fluid injection," *ARS Journal*, vol. 31, no. 12, pp. 1677–1685, 1961.

[16] G. Masuya, N. Chinzei, and S. Ishii, "Secondary gas injection into a supersonic conical nozzle," *AIAA Journal*, vol. 15, no. 3, pp. 301-302, 1977.

[17] R. D. Guhse, "An experimental investigation of thrust vector control by secondary injection," Tech. Rep. NASA CR-297, 1965.

[18] I. Zeierman and Y. Manheimer-Timnat, "Full control of solid propellant rockets by secondary injection," *Journal of Spacecraft and Rockets*, vol. 10, no. 3, pp. 161-162, 1973.

[19] T. Inouye and H. B. Nottage, "Experiments on rocket thrust vector control by hot gas injection," *Journal of Spacecraft and Rockets*, vol. 3, no. 5, pp. 737–739, 1966.

[20] M. Salehifar, M. Tahani, M. Hojaji, and A. Dartoomian, "CFD modeling for flow field characterization and performance analysis of HGITVC," *Applied Thermal Engineering*, vol. 103, pp. 291–304, 2016.

[21] C. Tian and Y. Lu, "Turbulence models of separated flow in shock wave thrust vector nozzle," *Engineering Applications of Computational Fluid Mechanics*, vol. 7, no. 2, pp. 182–192, 2014.

[22] R. Dhinagram and T. K. Bose, "Comparison of Euler and Navier stokes solutions for nozzle flows with secondary injection," in *34th Aerospace Sciences Meeting and Exhibit*, pp. 1–11, Reno, NV, USA, Janaury 1996, AIAA Paper 96-0453.

[23] H. Ko and W.-S. Yoon, "Performance analysis of secondary gas injection into a conical rocket nozzle," *Journal of Propulsion and Power*, vol. 18, no. 3, pp. 585–591, 2002.

[24] A. T. Sriram and J. Mathew, "Numerical prediction of two-dimensional transverse injection flows," in *42nd AIAA Aerospace Sciences Meeting and Exhibit*, Reno, NV, USA, 2004AIAA Paper No. 2004-1099.

[25] N. Vishnu, S. Vigneshwaran, S. Vignesh, C. Nichith, S. Sharan, and V. R. Sanal Kumar, "3D numerical studies on thrust vectoring using shock induced self impinging secondary jets," in *52nd AIAA/SAE/ASEE Joint Propulsion Conference*, Salt Lake City, UT, USA, 2016.

[26] V. Zmijanovic, V. Lago, M. Sellam, and A. Chpoun, "Thrust shock vector control of an axisymmetric conical supersonic nozzle via secondary transverse gas injection," *Shock Waves*, vol. 24, no. 1, pp. 97–111, 2014.

[27] L. Prince Raj, P. Rejith, and R. Balu, "Numerical simulation of a hot gas injection thrust vector control system performance," *Procedia Engineering*, vol. 38, pp. 1745–1749, 2012.

[28] S. S. Rajendran, T. R. Aravind Kumar, and K. S. Nareshkumar, "Studies on thrust vector control using secondary injection sonic and supersonic jets," in *Proceedings of 2nd International Conference on Mechanical, Electronics and Mechatronics Engineering*, pp. 17-18, London, UK, 2013.

[29] R. Deng, F. Kong, and H. D. Kim, "Numerical simulation of fluidic thrust vectoring in an axisymmetric supersonic nozzle," *Journal of Mechanical Science and Technology*, vol. 28, no. 12, pp. 4979–4987, 2014.

[30] E. Erdem and K. Kontis, "Numerical and experimental investigation of transverse injection flows," *Shock Waves*, vol. 20, no. 2, pp. 103–118, 2010.

[31] E. Erdem, K. Kontis, and S. Saravanan, "Penetration characteristics of air, carbon dioxide and helium transverse sonic jets in Mach 5 cross flow," *Sensors*, vol. 14, no. 12, pp. 23462–23489, 2014.

[32] F. Forghany, M. Taeibe-Rahni, and A. Asadollahi-Ghohieh, "Numerical investigation of optimization of injection angle effects on fluidic thrust vectoring," *Journal of Applied Fluid Mechanics*, vol. 10, no. 1, pp. 157–167, 2017.

[33] T. Chandra Sekar, A. Kushari, B. Mody, and B. Uthup, "Fluidic thrust vectoring using transverse jet injection in a converging nozzle with aft-deck," *Experimental Thermal and Fluid Science*, vol. 86, pp. 189–203, 2017.

[34] J. Shi, L. Zhou, Z. Wang, and X. Sun, "Investigation on flowfield characteristics and performance of shock vector control nozzle based on confined transverse injection," *Journal of Engineering for Gas Turbines and Power*, vol. 138, no. 10, p. 11, 2016.

[35] ANSYS/FLUENT, Inc, *Fluent 14.5 User Guide*, Fluent Inc, 2014.

[36] W. Huang, J.-G. Tan, J. Liu, and L. Yan, "Mixing augmentation induced by the interaction between the oblique shock wave and a sonic hydrogen jet in supersonic flows," *Acta Astronautica*, vol. 117, pp. 142–152, 2015.

[37] L.-Q. Li, W. Huang, and L. Yan, "Mixing augmentation induced by a vortex generator located upstream of the transverse gaseous jet in supersonic flows," *Aerospace Science and Technology*, vol. 68, pp. 77–89, 2017.

[38] O. P. Kostić, Z. A. Stefanović, and I. A. Kostić, "CFD modeling of supersonic airflow generated by 2D nozzle with and without an obstacle at the exit section," *FME Transaction*, vol. 43, no. 2, pp. 107–113, 2015.

[39] H. R. Noaman, H. B. Tang, and E. Khalil, "Numerical simulation of Nozzle flow field with secondary injection thrust vector control," in *2018 2nd International Conference on Mechanical, Material and Aerospace Engineering (2MAE 2018)*, vol. 179 of *MATEC Web of Conferences*, pp. 1–10, Wuhan, China, 201801003.

[40] H. Yamauchi, B. Choi, K. Takae, T. Kouchi, and G. Masuya, "Flowfield characteristics of a transverse jet into supersonic flow with pseudo-shock wave," *Shock Waves*, vol. 22, no. 6, pp. 533–545, 2012.

[41] N. B. Wood, "Calculation of the turbulent boundary layer in the nozzle of intermittent axisymmetric hypersonic wind tunnel," Tech. Rep. C.P.NO. 721, Aeronautical Research Council, 1964.

Journal of
Engineering

The Scientific World Journal

International Journal of
Rotating Machinery

Journal of
Sensors

Advances in
Multimedia

Advances in
Civil Engineering

Journal of
Control Science and Engineering

Journal of
Robotics

Journal of
Electrical and Computer Engineering

Advances in
OptoElectronics

VLSI Design

International Journal of
Navigation and Observation

Modelling & Simulation in Engineering

International Journal of
Aerospace Engineering

International Journal of
Chemical Engineering

International Journal of
Antennas and Propagation

Active and Passive Electronic Components

Shock and Vibration

Advances in
Acoustics and Vibration

Hindawi

Submit your manuscripts at
www.hindawi.com